



1

2

3 **Comparison of Global Observations and Trends of Total Precipitable Water Derived**
4 **from Microwave Radiometers and COSMIC Radio Occultation from 2006 to 2013**

5

6

7 Shu-peng Ho¹, Liang Peng¹, Carl Mears², Richard A. Anthes¹

8 ¹ University Corporation for Atmospheric Research, P.O. Box 3000, Boulder, CO. 80307-

9 3000

10 ² Remote Sensing Systems, Santa Rosa, California, USA,

11 Corresponding author address: Dr. Shu-Peng Ho, COSMIC Project Office, University

12 Corporation for Atmospheric Research, P. O. Box 3000, Boulder CO. 80307-3000

13 E-mail: spho@ucar.edu

14

15

16

17

18

20 Shu-Peng Ho, COSMIC Project Office, Univ. Corp. for Atmospheric Research, P. O.

21 Box 3000, Boulder CO. 80307-3000, USA (spho@ucar.edu)

22

23

24

25



26 **Abstract**

27 We compare atmospheric total precipitable water (TPW) derived from SSM/I (Special
28 Sensor Microwave Imager) and SSMIS (Special Sensor Microwave Imager Sounder)
29 radiometers and WindSat to collocated TPW estimates derived from COSMIC
30 (Constellation System for Meteorology, Ionosphere and Climate) radio occultation (RO)
31 under clear and cloudy conditions over the oceans from June 2006 to December 2013.
32 Results show that the mean microwave (MW) radiometer - COSMIC TPW differences
33 range from 0.06-0.18 mm for clear skies, 0.79-0.96 mm for cloudy skies, 0.46-0.49 mm for
34 cloudy but non-precipitation conditions, and 1.64-1.88 mm for precipitation conditions.
35 Because RO measurements are not significantly affected by clouds and precipitation, the
36 biases mainly result from MW retrieval uncertainties under cloudy and precipitating
37 conditions. All COSMIC and MW radiometers detect a positive TPW trend over these eight
38 years. The trend using all COSMIC observations collocated with MW pixels is 1.79
39 mm/decade, with a 95% confidence interval of (0.96, 2.63), which is in close agreement
40 with the trend estimated by all MW observations (1.78 mm/decade with a 95% confidence
41 interval of 0.94, 2.62). These two trends from independent observations are larger than
42 previous estimates and are a strong indication of the positive water vapor-temperature
43 feedback in a warming planet.

44

45

46

47

48



49 **1. Introduction**

50 Clouds are important regulators for Earth's radiation and hydrological balances.
51 Water vapor is a primary variable that affects cloud radiative effects and hydrological
52 feedbacks. Accurate observations of long-term water vapor under both clear and cloudy
53 skies are important for understanding the role of water vapor on climate, which is still one
54 of the largest uncertainties in understanding climate change mechanisms (IPCC 2013).
55 Trends in global and regional vertically integrated total atmospheric water vapor, or Total
56 Precipitable Water (TPW), are important indicators of climate warming because of the
57 strong positive feedback between temperature and water vapor increases. Accurate
58 observations of TPW are therefore important in identifying climate change and in verifying
59 climate models, which estimate a wide range of TPW trends (Roman et al. 2014).

60 The TPW depends on temperature (Trenberth and Guillemot, 1998; Trenberth et
61 al., 2005). Global TPW can be derived from satellite visible, infrared, and microwave
62 sensors (i.e., Wentz and Spencer, 1998; Fetzer et al. 2006; John and Soden, 2007; Fetzer
63 et al. 2008; Noël et al. 2004). However, no single remote sensing technique is capable of
64 completely fulfilling the needs for climate studies in terms of spatial and temporal
65 coverage and accuracy. For example, while water vapor retrievals from visible and
66 infrared satellite sensors are limited to clear skies over both lands and oceans, passive
67 microwave (MW) imagers on satellites can provide all sky water vapor products, but only
68 over oceans. These water vapor products are mainly verified by comparing to either
69 reanalysis, radiosonde measurements, or other satellite data (i.e., Soden, and Lanzante,
70 1996; Sohn and Smith, 2003; Noël et al. 2004; Palm et al. 2008; Sohn and Bennartz, 2008;
71 Wick et al. 2008; Milz et al. 2009; Prasad and Singh, 2009; Pougatchev et al. 2009;



72 Knuteson et al., 2010; Larar et al. 2010; Wang et al. 2010; Ho et al. 2010a, b). Results from
73 these validation studies show that the quality of water vapor data from different satellite
74 sensors varies under different atmospheric conditions. The change of reanalysis systems
75 and inconsistent calibration among data may also cause uncertainty in long-term stability
76 of water vapor estimates. In addition, it is well known that radiosonde sensor characteristics
77 can be affected by the changing environment (Luers and Eskridge, 1998; Wang and Zhang,
78 2008). Ho et al. (2010b) demonstrated that the quality of radiosonde humidity
79 measurements varies with sensor types, adding extra difficulties in making a consistent
80 validation of long term water vapor products.

81 MW imagers are among the very few satellite instruments that are able to provide
82 long-term (close to 30 years) all-weather time series of water vapor measurements using
83 similar sensors and retrieval techniques (Wentz, 2015). The measured radiances at 19.35,
84 22.235, and 37.0 GHz from SSMIS and 18.7, 23.8, and 37.0 GHz from WindSat are used
85 to derive TPW, total cloud water (TCW), wind speed, and rainfall rates over oceans (Wentz
86 and Spencer, 1998). These four variables are retrieved by varying their values until the
87 brightness temperatures calculated using a forward model match satellite-observed
88 brightness temperatures. Because MW radiation is significantly affected (absorbed or
89 scattered) by heavy rain, these four variables are only retrieved under conditions of no or
90 light-to-moderate rain (Schlüssel and Emery, 1990; Elsaesser and Kummerow, 2008;
91 Wentz and Spencer, 1998).

92 Recently version 7.0 daily ocean products mapped to a 0.25° grid derived from
93 multiple MW radiometers were released by Remote Sensing System (RSS) (Wentz, 2013).
94 Many validation studies have been performed by RSS by comparing the MW TPW



95 retrievals with those from ground-based Global Positioning System (gb-GPS) stations
96 (Mears et al, 2015; Wentz, 2015). Because the gb-GPS stations are nearly always located
97 on land, these validation studies use stations located on small and isolated islands (Mears
98 et al., 2015). RSS results for TPW collocated with those derived from gb-GPS over these
99 island stations show that their mean differences vary from station to station, and can be as
100 large as 2 mm. The mean difference also varies with surface wind speed, varying from 1
101 mm at low wind speeds to -1 mm at high wind (20 m/s) speeds. The difference is near zero
102 for the most common wind speeds (6 to 12 m/s). Because the uncertainty of the input
103 parameters and change of antenna for each GPS receiver (Bock et al., 2013), the mean
104 TPW(RSS) – TPW (gb-GPS) can vary from -1.5 mm to 1.5 mm for a single MW radiometer
105 (see Figure 4 in Mears et al., 2015). Wentz (2015) compared 17 years of Tropical Rainfall
106 Measuring Mission (TRMM) Microwave Imager (TMI) TPW collocated with gb-GPS
107 TPW over the region from 45°N to 45° S. The mean TMI- gb-GPS TPW bias was estimated
108 to be 0.45 mm with a standard deviation (σ) of 2.01 mm.

109 Unlike passive MW radiometers and infrared sensors, radio occultation (RO) is an
110 active remote sensing technique. RO can provide all-weather, high vertical resolution (from
111 ~100 m near the surface to ~1.5 km at 40 km) refractivity profiles (Anthes, 2011). The
112 basics of the RO measurement is a timing measured against reference clocks on the ground,
113 which are timed and calibrated by the atomic clocks at the National Institutes for Standards
114 and Technology (NIST). With a GPS receiver onboard the LEO (Low-Earth Orbiting)
115 satellite, this technique is able to detect the bending of radio signals emitted by GPS
116 satellites and traversing the atmosphere. With the information about the relative motion of
117 the GPS and LEO satellites, the bending angle profile of the radio waves can be used to



118 derive all-weather refractivity, pressure, temperature, and water vapor profiles in the
119 neutral atmosphere (Anthes et al., 2008).

120 Launched in June 2006, COSMIC (Constellation Observing System for
121 Meteorology, Ionosphere, and Climate) RO data have been used to study atmospheric
122 temperature and refractivity trends in the lower stratosphere (Ho et al., 2009a, b, and 2012),
123 and modes of variability above, within, and below clouds (Biondi et al., 2012, 2013; Teng
124 et al., 2013; Scherllin-Pirscher et al., 2012; Zeng et al., 2012; Mears et al., 2012). Wick et
125 al., (2008) (Wick2008 hereafter) demonstrated the feasibility of using COSMIC-derived
126 TPW to validate SSM/I TPW products over the east Pacific Ocean using one month of
127 data. Many studies have demonstrated the usefulness of RO derived water vapor to detect
128 climate signals of El Niño–Southern Oscillation (ENSO; Teng et al., 2013; Scherllin-
129 Pirscher et al, 2012; Huang et al., 2013), Madden-Julian Oscillation (MJO; Zeng et al.,
130 2012), and improving moisture analysis of atmospheric rivers (Neiman et al., 2008; Ma et
131 al. 2011).

132 The objective of this study is to use COSMIC RO TPW to characterize the global
133 TPW values and trends derived from multiple MW radiometers over oceans, including
134 under cloudy and precipitating skies. COSMIC TPW from June 2006 to December 2013
135 are compared to the co-located TPW derived from MW radiometers over the same time
136 period. Because RO data are not strongly sensitive to clouds and precipitation, COSMIC
137 TPW estimates can be used to identify possible MW TPW biases under different
138 meteorological conditions. We describe datasets and analysis method used in the
139 comparisons in Section 2. The comparison results under clear skies and cloudy skies are



140 summarized in Sections 3 and 4, respectively. The time series analysis is in Section 5. We
141 conclude this study in Section 6.

142

143 **2. RSS Version 7.0 Data and COSMIC TPW Data and Comparison Method**

144 **2.1 RSS Version 7.0 Data Ocean Products**

145 The RSS version 7.0 ocean products are available for SSM/I, SSMIS, AMSR-E,
146 WindSat, and TMI. The inversion algorithm is mainly based on Wentz and Spencer,
147 (1998), where above a cutoff in liquid water column, water vapor is no longer
148 retrieved. The various radiometers from the different satellites have been precisely inter-
149 calibrated at the radiance level by analyzing the measurements made by pairs of satellites
150 operated at the same time. This was done for the explicit purpose of producing versions of
151 the datasets that can be used to study decadal-scale changes in TPW, wind, clouds, and
152 precipitation, so special attention was focused on inter-annual variability in instrument
153 calibration. The calibration procedures and physical inversion algorithm used to
154 simultaneously retrieve TPW, surface wind speed (and thereby surface wind stress and
155 surface roughness) and the total liquid water content are summarized in Wentz (2013) and
156 Wentz (1997), respectively. This allows the algorithm to minimize the effect of wind speed,
157 clouds, and rain on the TPW measurement.

158 The RSS version 7.0 daily data are available on a $0.25^\circ \times 0.25^\circ$ grid for daytime and
159 nighttime (i.e., 1440x720x2 daily per day). Figures 1a-d shows the RSS V7.0 monthly
160 mean F16 SSMIS TPW (in mm), surface skin temperature (in K), liquid water path (LWP,
161 in mm), and rain rate (RR, in mm/hour), respectively. Figure 1 shows that the variation and
162 distribution of TPW over oceans (Fig. 1a) is, in general, closely linked to surface skin



163 temperature (Fig. 1b), which is modulated by clouds and the hydrological cycle (Soden et
164 al., 2002). The distribution of monthly TPW is consistent with those of cloud water vapor
165 distribution patterns where highest TPW values (and LWP and RR) occur in persistent
166 cloudy and strong convective regions over the tropical west Pacific Ocean near Indonesia.

167 Because COSMIC reprocessed TPW data are only available from June 2006 to
168 December 2013 (i.e., COSMIC2013), the SSM/I F15, SSMIS F16, SSMIS F17, together
169 with WindSAT RSS Version 7.01 ocean products covering the same time period are used
170 in this study. Table 1 summarizes the starting date and end date for RSS SSM/I F15, SSMIS
171 F16, SSMIS F17, and WindSAT data. The all sky daily RSS ocean products for F15, F16,
172 F17, and WindSat are downloaded from <http://www.remss.com/missions/ssmi>.

173

174 **2.2 COSMIC TPW Products**

175 The atmospheric refractivity N is a function of the pressure P , temperature T , water
176 vapor pressure P_w , and water content W through the following relationship (Kursinski
177 1997; Zou et al. 2012):

178

$$179 \quad N = 77.6 \frac{P}{T} + 3.73 \times 10^5 \frac{P_w}{T^2} + 1.4W_{\text{water}} + 0.61W_{\text{ice}} \quad (1)$$

180

181 where P is pressure in hPa, T is temperature in K, P_w is water vapor pressure in hPa,
182 W_{water} is liquid water content in grams per cubic meter (gm^{-3}), and W_{ice} is the ice water
183 content in gm^{-3} . The last two terms generally contribute less than 1% to the refractivity and
184 may be ignored (Zou et al., 2012). However, they can be significant for some applications
185 under conditions of high cloud liquid or ice water content, as shown by Lin et al. 2010;



186 Yang and Zou 2012; Zou et al. 2012. We will neglect these terms in this study, but because
187 we are looking at small differences between MW and RO TPW in cloudy and precipitating
188 conditions in this paper, we estimate the possible contribution of these terms to RO TPW
189 and the consequences of neglecting them here. Since both of these terms increase N,
190 neglecting them in an atmosphere in which they are present will produce a small positive
191 bias in water vapor pressure P_w and therefore total precipitable water when integrated
192 throughout the entire depth of the atmosphere.

193 Typical value of cloud LWC range from $\sim 0.2 \text{ gm}^{-3}$ in stratiform clouds (Thompson,
194 2007) to 1 gm^{-3} in convective clouds (Thompson, 2007; Cober et al. 2001). Extreme values
195 may reach $\sim 2 \text{ gm}^{-3}$ in deep tropical convective clouds (i.e., cumulonimbus). Ice water
196 content values are smaller, typically $0.01 - 0.03 \text{ gm}^{-3}$ (Thompson, 2007).

197 For extremely high values of W_{water} and W_{ice} of 2.0 and 0.5 gm^{-3} , the contributions
198 to N are 2.8 and 0.3 respectively. The values of N in the atmosphere decrease exponentially
199 upward, from ~ 300 near the surface to ~ 150 at $P=500 \text{ hPa}$. Using the above extreme values
200 at 500 hPa , W_{water} may contribute from up to 1.6% of N and W_{ice} up to 0.2%. Thus we may
201 assume that in most cases the error in N due to neglecting these terms will be less than 1%.
202 The effect on TPW will be even less, since clouds do not generally extend through the full
203 depth of the atmosphere. Finally, the $\sim 200 \text{ km}$ horizontal averaging scale of the RO
204 observation footprint makes it unlikely that such extremely high values of water and ice
205 content will be present over this scale. We conclude that the small positive bias in RO TPW
206 introduced by neglecting the liquid and water terms in (1) will be less than 1%.

207 To resolve the ambiguity of COSMIC refractivity associated with both temperature
208 and water vapor in the lower troposphere a 1D-var algorithm ([9](http://cosmic-</p></div><div data-bbox=)



209 io.cosmic.ucar.edu/cdaac/doc/documents/1dvar.pdf) is used to derive optimal temperature
210 and water vapor profiles while temperatures and water vapor profiles from the ERA-
211 Interim reanalysis are used as a priori estimates (Neiman et al. 2008; Zeng et al. 2012).

212 Note that because RO refractivity is very sensitive to water vapor variations in the
213 troposphere (Ho et al. 2007), and is less sensitive to temperature errors, RO-derived water
214 vapor product is of high accuracy (Ho et al. 2010 a, b). It is estimated that 1K of
215 temperature error will introduce less than 0.25 g/kg of water vapor bias in the troposphere
216 in the 1D-var retrievals. Although the first guess temperature and moisture are needed for
217 the 1D-Var algorithm, the retrieved water vapor profiles are insensitive to the first guess
218 water vapor profiles (Neiman et al. 2008).

219 The horizontal footprint of a COSMIC observation is about 200 km in the lower
220 troposphere and its vertical resolution is about 100 m near the surface and 1.5 km at 40 km.
221 The COSMIC post-processed water vapor profiles version 2013.2640 collected from
222 COSMIC Data Analysis and Archive Center (CDAAC)
223 (<http://cosmicio.cosmic.ucar.edu/cdaac/index.html>) are used to construct the COSMIC
224 TPW data. To further validate the accuracy of COSMIC-derived water vapor, we have
225 compared COSMIC TPW with those derived from ground-based GPS (i.e., International
226 Global Navigation Satellite Systems–IGS, Wang et al. 2007) which are assumed to be
227 independent of location. Only those COSMIC profiles whose lowest penetration heights
228 are within 200 meters of the height of ground-based GPS stations are included. Results
229 showed that the mean global difference between IGS and COSMIC TPW is about -0.2 mm
230 with a standard deviation of 2.7 mm (Ho et al., 2010a). Similar comparisons were found
231 by Teng et al. (2013) and Huang et al. (2013).



232 **2.3 Preparation of COSMIC TPW data for Comparison**

233 In this study, only those COSMIC water vapor profiles penetrating lower than 0.1
234 km are integrated to compute TPW. To compensate for the water vapor amount below the
235 penetration height, we follow the following procedure:

- 236 i) we assume the relative humidity below the penetration height is equal to 80%. This is
237 a good assumption especially over oceans near the sea surface (Mears et al., 2015);
- 238 ii) the temperatures below the penetration height are taken from the ERA-interim
239 reanalysis;
- 240 iii) we compute the water vapor mixing ratio below the penetration heights;
- 241 iv) we integrate the TPW using COSMIC water vapor profiles above the penetration
242 heights with those water vapor profile below the penetration heights.

243 Pairs of MW and RO TPW estimates collocated within 50 km and one hour are collected.
244 Wick2008 used MW-RO pairs within 25 km and one hour in time. To evaluate the effect
245 of the spatial difference on the TPW difference, we also computed TPW differences for
246 MW-RO pairs within 75 km, 100 km, and 150 km, and 200 km. We found the larger spatial
247 difference increases the mean TPW biases slightly to +/- 0.25 mm and the standard
248 deviations to +/- 1.91 mm, which is likely because of the high spatial variability of water
249 vapor.

250 With a $0.25^\circ \times 0.25^\circ$ grid, there are about 20 to 60 MW pixels matching one
251 COSMIC observation. The number of pixels varies at different latitudes. A clear MW-RO
252 pair is defined as instances when *all* the TCW values for the collocated MW pixels are
253 equal to zero. A cloudy MW-RO ensemble is defined as instances when *all* the TCW values
254 from the collocated MW pixels are larger than zero. Partly cloudy conditions (some of



255 pixels zero and some non-zero) are excluded from this study. The cloudy ensembles are
256 further divided into precipitating and non-precipitating conditions. MW-RO pairs are
257 defined as cloudy non-precipitating when less than 20% of MW pixels have rainfall rates
258 larger than zero mm/hour. Cloudy precipitating MW-RO pairs are defined when more than
259 20% of the pixels have rainfall rates larger than zero. Because microwave radiances are not
260 sensitive to ice, we treat cloudy pixels of low density like cirrus clouds as clear pixels.

261

262 **3. Comparison of MW and RO TPW with clear skies**

263 In total there are 26,678 F15-RO pairs, 31,610 F16-RO pairs, 31,291 F17-RO pairs,
264 and 21,996 WindSat-RO pairs from June 2006 to Dec. 2013, respectively. Because
265 microwave radiances are not sensitive to ice, we treat cloudy pixels of low density like
266 cirrus clouds as clear pixels. Figures 2a-d show scatter plots for F15-COSMIC TPW, F16-
267 COSMIC TPW, F17-COSMIC TPW, and WindSat-COSMIC TPW under clear skies.
268 Figures 3a-d show that MW clear sky TPW from F15, F16, F17, and WindSat are all very
269 consistent with those from co-located COSMIC observations. As summarized in Table 2,
270 under clear conditions where SSM/I provides high quality TPW estimates, the mean TPW
271 biases between F16 and COSMIC (F16- COSMIC) is equal to 0.03 mm with a standard
272 deviation σ of 1.47 mm. The mean TPW differences are equal to 0.06 mm with a σ of 1.65
273 mm for F15, 0.07 mm with a σ of 1.47 mm for F17, and 0.18 mm with a σ of 1.35 mm for
274 WindSat. The reason for larger standard deviation for F15 may be because the F15 data
275 after August 2006 were corrupted by the “rad-cal” beacon that was turned on at this time
276 (Hilburn and Wentz, 2008). F16 had solar radiation intrusion into the hot load during the
277 time period, while F17 and WindSat had no serious issues.



278

279 4. Global comparisons of MW and RO TPW with cloudy skies**280 4.1 Comparison of MW, RO, and Ground-based GPS TPW**

281 Figures 3a-c depict the scatter plots for F16-COSMIC pairs under cloudy, cloudy
282 non-precipitation, and precipitation conditions from June 2006 to December 2013 over
283 oceans. While there is a very small bias (0.031 mm) for clear pixels (Fig. 2b), there is a
284 significant positive TPW bias (0.794 mm) under cloudy conditions (Fig. 3a). This may
285 explain the close to 0.4 mm mean TMI-gb GPS TPW biases found by Wentz et al., (2015)
286 where a close to 7 years of data were used. Figure 3c depicts that the large SSM/I TPW
287 biases under cloudy skies are mainly from the pixels with precipitation (mean bias is equal
288 to 1.825 mm) although precipitation pixels are of about less than 6% of the total F16-
289 COSMIC pairs. Because RO measurements are not significantly affected by clouds and
290 precipitation, the biases mainly result from MW retrieval uncertainty under cloudy
291 conditions. The fact that the MW-COSMIC biases for precipitation conditions (1.825 mm,
292 Fig. 3c and 1.62-1.88 mm in Table 2) is much larger than those for cloudy, but non-
293 precipitation conditions, indicates that significant scattering and absorbing effects are
294 present in the passive MW measurements when it rains. The correlation coefficients for
295 F15-RO, F16-RO, F17-RO, and WindSat-RO pairs for all sky conditions are all larger than
296 0.96 (not shown).

297 MW and gb-GPS TPW comparisons show similar differences as the MW-RO
298 differences under the different sky conditions. We compared F16 pixels with those from
299 gb-GPS within 50 km and 1 hour over the 33 stations studied by Mears et al. (2015) from
300 2002 to 2013. Figs. 4a-d depicts the scatter plots for F16-gb-GPS TPW under clear, cloudy,



301 cloudy non-precipitating, and cloudy precipitating conditions, respectively. The F16-gb-
302 GPS mean biases are equal to 0.241 mm (clear skies), 0.614 mm (cloudy skies), 0.543 mm
303 (cloudy-non precipitation) and 1.197 mm (precipitation), which are similar to those
304 estimated from MW-RO comparisons (Table 2).

305 The above results show that the MW estimates of TPW are biased positively
306 compared to both the RO and the ground-based GPS estimates, which are independent
307 measurements. The biases are smallest for clear skies and largest for precipitating
308 conditions, with cloudy, non-precipitating biases in between. Overall, the results suggest
309 that clouds and especially precipitation contaminate the MW radiometer measurements to
310 a small but significant degree.

311

312 **4.2 Time Series of MW, RO, and Ground-based TPW Biases under Various** 313 **Meteorological Conditions**

314 To further examine how rain and cloud drops affect the MW TPW retrievals, we
315 show how the F16-RO TPW biases vary under different meteorological conditions in Fig.
316 5. The bias dependence on wind speed (Fig. 5a) is small. Unlike the results from Mears et
317 al., (2015), the mean TPW biases between F16 and COSMIC are within 0.5 mm with high
318 winds (wind speed larger than 20 m/s). Fig. 5b indicates that the F16-COSMIC bias is
319 larger with TPW greater than about 10 mm, which usually occurs under cloudy conditions.
320 The F16-COSMIC biases can be as large as 2.0 mm when the rainfall rate is larger than 1
321 mm/hour (Fig. 5c), which usually occurs with high total liquid cloud water (Fig. 5d)
322 conditions. The F16 TPW biases can be as large as 2 mm when total cloud water is larger
323 than 0.3 mm (Fig. 5d). Fig. 5e shows that the larger F16-COSMIC TPW biases (2-3 mm)



324 mainly occur over regions with surface skin temperature less than 270 K (higher latitudes,
325 see Figure 1b). The F15, F17, and WindSat TPW biases under different meteorological
326 conditions are very similar to those of F16 (not shown).

327 In Figure 6 we compare RSS V7.0 F16 MW TPW to the ground-based GPS TPW
328 over various meteorological conditions. The magnitudes of the MW-gb-GPS TPW
329 differences under high rain rate and high total cloud water conditions are somewhat smaller
330 than those of MW-RO pairs (varying from about 0.5 mm to 2.0 mm), which may be because
331 most of the MW-gb-GPS samples are collected under low rain rates (less than 1 mm/hour)
332 conditions.

333

334 **5. Eight Year Time Series and Trend Analysis under All Skies**

335 **5.1 Monthly Mean TPW Time Series Comparison**

336 To further examine MW TPW long-term stability and trend uncertainty due to rain
337 and water drops for different instruments, we compared time series of the MW and
338 COSMIC monthly mean TPW differences from June 2006 to Dec. 2013. Figures 7a-d show
339 the monthly mean F16-COSMIC TPW differences from June 2006 to Dec. 2013 for clear,
340 cloudy, cloudy non-precipitation, and precipitation conditions. In general, the microwave
341 TPW biases under different atmospheric conditions are positive and stable from June 2006
342 to Dec. 2013, as reflected in relatively small standard deviation values (Table 3). Except
343 for F15, the standard deviations of the monthly mean TPW anomaly range are less than
344 0.38 mm (Table 3). In contrast, the F15-COSMIC monthly mean σ range from 0.48 mm to
345 0.69 mm with different conditions.



346 Table 3 also shows the trend in the RO estimates of TPW over the eight-year period
347 of study. The trends are range from -0.12 mm/decade (WindSat, clear skies) to 2.52
348 mm/decade (F15, precipitation conditions). The overall trend is positive as discussed in the
349 next section. Table 3 shows that in general the trends are more strongly positive under
350 cloudy and precipitation conditions compared to clear conditions.

351

352 **5.2 De-seasonalized Trends of MW-RO Differences and TPW**

353 Fig. 8 depicts the de-seasonalized trends of the MW-RO TPW differences under
354 cloudy skies for F15 (Fig. 8a), F16 (Fig. 8b), F17 (Fig. 8c), and Windsat (Fig.8d). Except
355 for F15, the de-seasonalized trends of the MW-RO TPW differences for the MW
356 radiometers are close to zero, indicating little change over these eight years. The trends of
357 the biases associated with F16, F17, F18 and WindSat under all sky conditions range from
358 -0.09 to 0.27 mm/decade (details not shown).

359 The reason for larger standard deviations of the MW minus RO differences for F15
360 (Tables 2 and 3 and Fig. 8a) is very likely because the F15 data after August 2006 were
361 corrupted by the “rad-cal” beacon that was turned on at this time. Adjustments were derived
362 and applied to reduce the effects of the beacon, but the final results still show excess noise
363 relative to uncorrupted measurements (Hilburn and Wentz, 2008). RSS does not
364 recommend using these measurements for studies of long-term change. Thus we consider
365 the F15 data less reliable during the period of our study.

366 Fig. 9 shows the de-seasonalized time series of global monthly mean TPW for all
367 MW radiometers and COSMIC under all sky conditions. The close to eight year trends for
368 TPW estimated from both passive MW radiometers and active COSMIC RO sensors are



369 positive and very similar in magnitude. The global mean trend of COSMIC RO TPW is
370 1.79 mm/decade with a 95% confidence interval of (0.96, 2.63) mm/decade while the
371 global mean trend from all the MW estimates is 1.78 mm/decade with a 95% confidence
372 interval of (0.94, 2.62). This close agreement between completely independent
373 measurements lends credence to both estimates.

374 The positive trends in TPW from the independent MW and RO measurements
375 reflect the positive feedback between TPW and global warming and are considerably
376 greater than previous estimates over other time periods. For example, Durre et al. (2009)
377 estimated a trend of 0.45 mm/decade for the Northern Hemisphere over the period 1973-
378 2006. Trenberth et al. (2005) estimated a global trend of 0.40 +/- 0.09 mm/decade for the
379 period 1988 to 2001. The 100-year trend in global climate models is variable, ranging from
380 0.55 to 0.72 mm/decade (Roman et al., 2014).

381 Although both MW and RO measurements demonstrate positive trends in TPW
382 from 2006 to 2013, the trends in TPW vary over different regions. Fig. 10 shows the global
383 map of TPW trend over oceans using all F16, F17, and WindSat data from 2006 to 2013.
384 Fig. 10 shows that the positive trends in TPW exist mainly over central and north Pacific
385 oceans, south of China and west of Australia, south of South American, and east of
386 America.

387

388 **6. Discussion and conclusions**

389 RSS water vapor products have been widely used for climate research. The newly
390 available RSS V7.0 data products have been processed using consistent calibration
391 procedures (Wentz, 2013). This was done for the explicit purpose of producing versions of



392 the datasets that can used to study decadal scale changes in TPW, wind, clouds, and
393 precipitation. These water vapor products are mainly verified by comparing to either
394 reanalysis, radiosondes measurements, or other satellite data. However, because the quality
395 of these datasets may also vary under different atmospheric conditions, the uncertainty in
396 long-term water vapor estimates may still be large. In this study, we used TPW estimates
397 derived from COSMIC active RO sensors to identify TPW uncertainties from four different
398 MW radiometers under clear, cloudy, cloudy/non-precipitation, and cloudy/precipitation
399 skies over nearly eight years (from June 2006 to Dec. 2013). Because RO data are not
400 sensitive to clouds and precipitation, RO-derived water vapor products are useful to
401 identify the possible TPW biases retrieved from measurements of passive microwave
402 imagers under different sky conditions. We reach the following conclusions:

403 1) Clear sky biases: The collocated COSMIC RO TPW estimates under clear skies
404 are highly consistent with the MW TPW estimates under clear sky conditions (within +/-
405 0.2 mm and with a correlation coefficient greater than 0.96). The mean TPW bias between
406 F16 and COSMIC (F16- COSMIC) is equal to 0.03 mm with a standard deviation σ of 1.47
407 mm. The mean TPW differences are equal to 0.06 mm with a σ of 1.65 mm for F15, 0.07
408 mm with a σ of 1.47 mm for F17, and 0.18 mm with a σ of 1.35 mm for WindSat. These
409 small values give us confidence in our approach to interpolate COSMIC data the last few
410 hundred meters below the lowest penetration height. The consistent F15-COSMIC, F16-
411 COSMIC, F17-COSMIC, and WindSat-COSMIC TPW under clear skies also show that
412 COSMIC TPW can be used as good references to identify and correct TPW among
413 different MW imagers for other sky conditions.



414 2) Biases under cloudy skies: while there are very small biases for clear pixels,
415 there are significant positive MW TPW biases (~ 0.80 mm) under cloudy conditions when
416 compared to RO TPW. The large SSM/I TPW biases under cloudy skies result mainly from
417 the pixels with precipitation. The mean bias is equal to 1.83 mm for COSMIC-F16 pairs,
418 which is much larger than the bias for cloudy, but non-precipitation conditions. This
419 indicates that the significant scattering and absorbing effects are present in the passive MW
420 measurements when it rains. The F16 – Ground-based GPS mean biases are equal to 0.24
421 mm (for clear skies), 0.61 mm (for cloudy skies), 0.54 mm (for cloudy-non precipitation)
422 and 1.2 mm (for precipitation) which are consistent with those from F16-COSMIC
423 comparisons.

424 3) Biases among different instruments: using RO TPW estimates collocated with
425 different MW instruments, we are able to identify possible TPW inconsistencies among
426 MW instruments even they are not collocated. The de-seasonalized trends in MW-RO TPW
427 differences for three MW radiometers (i.e., F16, F17, and WindSat) are close to zero,
428 indicating consistency among these radiometers. However, the F15-COSMIC differences
429 are larger and show a significant trend over the eight years of the study. It is likely that F15
430 data after August 2006 were corrupted by the “rad-cal” beacon that was turned on at this
431 time.

432 4) Trend of TPW under all skies: The eight-year trends of TPW estimated from
433 both passive MW radiometer and active COSMIC sensors show increasing TPW globally,
434 with higher trends under cloudy conditions. The global mean trend of COSMIC RO TPW
435 collocated with MW observations is 1.79 mm/decade with a 95% confidence interval of
436 (0.96, 2.63) mm/decade. The global mean trend from all the MW estimates is 1.78



437 mm/decade with a 95% confidence interval of (0.94, 2.62). This close agreement between
438 completely independent measurements lends credence to both estimates. These trends are
439 significantly higher than other estimates and are a strong confirmation of the water vapor-
440 temperature feedback in a warming global atmosphere.

441

442 **Acknowledgements.** This work is supported by the NSF CAS AGS-1033112. We thank
443 Eric DeWeaver (NSF) and Jack Kaye (NASA) for sponsoring this work.

444

445

446

447

448

449

450

451

452

453

454

455

456

457

458

459



460 **References**

- 461 Anthes, R. A., P. Bernhardt, Y. Chen, L. Cucurull, K. Dymond, D. Ector, S. Healy, S.-P.
462 Ho, D. Hunt, Y.-H. Kuo, H. Liu, K. Manning, C. McCormick, T. Meehan, W. Randel,
463 C. R. Rocken, W. Schreiner, S. Sokolovskiy, S. Syndergaard, D. Thompson, K.
464 Trenberth, T.-K. Wee, Z. Zeng, 2008: The COSMIC/FORMOSAT-3 Mission: Early
465 Results, *Bul. Amer. Meteor. Sci.* 89, No.3, 313-333, DOI: 10.1175/BAMS-89-3-313.
- 466 Anthes, R.A., 2011: Exploring Earth's atmosphere with radio occultation: contributions to
467 weather, climate and space weather. *Atmos. Meas. Tech.*, 4, 1077-1103,
468 DOI:10.5194/amt-4-1077-2001.
- 469 Biondi, R., W. Randel, S.-P. Ho, T. Neubert, and S. Syndergaard, 2012: Thermal
470 structure of intense convective clouds derived from GPS radio occultations. *Atmos.*
471 *Chem. Phys.*, doi:10.5194/acp-12-5309-2012.
- 472 Biondi, R., S.-P. Ho, W. Randel, T. Neubert and S. Syndergaard, 2013: Tropical cyclone
473 cloud-top heights and vertical temperature structure detection using GPS radio
474 occultation measurements, *J. Geophys. Research*, VOL. 118, 1–13,
475 doi:10.1002/jgrd.50448.
- 476 Bock, O., Bossler, P., Bourcy, T., David, L., Goutail, F., Hoareau, C., Keckhut, P.,
477 Legain, D., Pazmino, A., Pelon, J., Pipis, K., Poujol, G., Sarkissian, A., Thom, C.,
478 Tournois, G., and Tzanos, D. 2013: Accuracy assessment of water vapour
479 measurements from in situ and remote sensing techniques during the DEMEVAP
480 2011 campaign at OHP, *Atmos. Meas. Tech.*, 6, 2777–2802, doi:10.5194/amt-6-
481 2777-2013.
- 482 Cober, S. G., G. A. Isaac, and J. W. Strapp, 2001: Characterizations of aircraft icing



- 483 environments that include supercooled large drops. *J. Appl. Meteor.*, 40, 1984–2002.
- 484 Durre, I., C. N. Williams Jr., X. Yin, and R. S. Vose, 2009: Radiosonde-based trends in
485 precipitable water over the Northern Hemisphere: An update, *J. Geophys. Res.*, 114,
486 D05112, doi:10.1029/2008JD010989.
- 487 Elsaesser, G. S. and C. D. Kummerow, 2008: Towards a fully parametric retrieval of the
488 non-raining parameters over the global ocean. *J. Appl. Meteor. & Climatol.*, 47, 1590
489 – 1598.
- 490 Fetzer, E. J., B. H. Lambrigtsen, A. Eldering, H. H. Aumann, and M.T. Chahine, M.T.,
491 2006: Biases in total precipitable water vapor climatologies from atmospheric infrared
492 sounder and advanced microwave scanning radiometer. *J. Geophys. Res.*, 111,
493 D09S16, doi: 10.1029/2005JD006598.
- 494 Fetzer, E. J. W.G. Read, and D. Waliser, 2008: Comparison of upper tropospheric water
495 vapor observations from the Microwave Limb Sounder and Atmospheric Infrared
496 Sounder. *J. Geophys. Res.*, 113/D22, D22110.
- 497 Hilburn, K. A., F. J. Wentz, 2008: Mitigating the impact of RADCAL beacon
498 contamination on F15 SSM/I ocean retrievals, *Geophysical Research Letters*, 35,
499 L18806, doi:10.1029/2008GL034914.
- 500 Ho, S.-P., Kuo, Y.-H., and Sokolovskiy, S., 2007: Improvement of the temperature and
501 moisture retrievals in the lower troposphere using AIRS and GPS radio occultation
502 measurements. *J. Atmos. Oceanic Technol.*, 24, 1726-1739,
503 doi:10.1175/JTECH2071.1.
- 504 Ho, S.-P., G. Kirchengast, S. Leroy, J. Wickert, A. J. Mannucci, A. K. Steiner, D. Hunt,
505 W. Schreiner, S. Sokolovskiy, C. O. Ao, M. Borsche, A. von Engeln,



- 506 U. Foelsche, S. Heise, B. Iijima, Y.-H. Kuo, R. Kursinski, B. Pirscher, M. Ringer, C.
507 Rocken, and T. Schmidt, 2009a: Estimating the Uncertainty of using GPS Radio
508 Occultation Data for Climate Monitoring: Inter-comparison of CHAMP Refractivity
509 Climate Records 2002-2006 from Different Data Centers, *J. Geophys.*
510 *Res.*, doi:10.1029/2009JD011969.
- 511 Ho, S.-P., M. Goldberg, Y.-H. Kuo, C.-Z. Zou, W. Schreiner, 2009b: Calibration of
512 Temperature in the Lower Stratosphere from Microwave Measurements using
513 COSMIC Radio Occultation Data: Preliminary Results, *Terr. Atmos. Oceanic Sci.*,
514 Vol. 20, doi: 10.3319/TAO.2007.12.06.01(F3C).
- 515 Ho, S.-P., Y.-H. Kuo, W. Schreiner, X. Zhou, 2010a: Using SI-traceable Global Positioning
516 System Radio Occultation Measurements for Climate Monitoring [In “States of the
517 Climate in 2009]. *Bul. Amer. Meteor. Sci.*, 91 (7), S36-S37.
- 518 Ho, S.-P., Zhou X., Kuo Y.-H., Hunt D., Wang J.-H., 2010b: Global Evaluation of
519 Radiosonde Water Vapor Systematic Biases using GPS Radio Occultation from
520 COSMIC and ECMWF Analysis. *Remote Sensing*. 2010; 2(5):1320-1330.
- 521 Ho, S.-P., D. Hunt, A. K. Steiner, A. J. Mannucci, G. Kirchengast, H. Gleisner, S. Heise,
522 A. von Engeln, C. Marquardt, S. Sokolovskiy, W. Schreiner, B. Scherllin-Pirscher,
523 C. Ao, J. Wickert, S. Syndergaard, K. B. Lauritsen, S. Leroy, E. R. Kursinski, Y.-H.
524 Kuo, U. Foelsche, T. Schmidt, and M. Gorbunov, 2012: Reproducibility of GPS
525 Radio Occultation Data for Climate Monitoring: Profile-to-Profile Inter-comparison
526 of CHAMP Climate Records 2002 to 2008 from Six Data Centers, *J. Geophys.*
527 *Research*. VOL. 117, D18111, doi:10.1029/2012JD017665.
- 528 Huang, C.-Y., W.-H. Teng, S.-P. Ho, Y.-H. Kuo, 2013: Global Variation of COSMIC



- 529 Precipitable Water over Land: Comparisons with Ground-based GPS Measurements
530 and NCEP Reanalyses, *Geophysical Research Letters*, DOI: 10.1002/grl.50885.
- 531 IPCC, 2013: Climate Change 2013: The Physical Science Basis. Contribution of Working
532 Group I to the Fifth Assessment Report of the Intergovernmental Panel on Climate
533 Change (IPCC). Cambridge University Press, Cambridge, United Kingdom and New
534 York, NY, USA, 1535 pp, doi:10.1017/CBO9781107415324.
- 535 John, V. O. and B.J. Soden, 2007: Temperature and humidity biases in global climate
536 models and their impacts on climate feedbacks. *Geophysical Research Letters*, 34,
537 L18605, doi:10.1029/2007GL030736.
- 538 Knuteson, R., S. Bedka, J. Roman, D. Tobin, D. Turner, and H. Revercomb, 2010: AIRS
539 and IASI Precipitable Water Vapor (PWV) Absolute Accuracy at Tropical, Mid-
540 Latitude, and Arctic Ground-Truth Sites. Presented at the International TOVS Study
541 Conference, Monterey, CA, USA, 14-10 April 2010, available online at
542 <http://cimss.ssec.wisc.edu/itwg/itsc/itsc17/>.
- 543 Kursinski, E.R., G.A. Hajj, J.T. Schofield and R.P. Linfield, 1997: Observing Earth's
544 atmosphere with radio occultation measurements using the Global Positioning
545 System. *J. Geophys. Res.* 102, No. D19, 23,429-23,465.
- 546 Larar, A. M., W. L. Smith, D. K. Zhou, X. Liu, H. Revercomb, J. P. Taylor, S. M. Newman,
547 and P. Schlüssel, 2010: IASI spectral radiance validation inter-comparisons: case study
548 assessment from the JAIVEx field campaign, *Atmos. Chem. Phys.*, 10, 411-430.
- 549 Lin, L., X. Zou, R. Anthes, and Y.-H. Kuo, 2010: COSMIC GPS cloudy profiles. *Mon.*
550 *Wea. Rev.*, 138, 1104–1118.
- 551 Luers, J. K. and R.E. Eskridge, 1998: Use of radiosonde temperature data in climate



- 552 studies. *J. of Climate*, 11, 1002–1019.
- 553 Ma, Z., Y.-H. Kuo, F. M. Ralph, P. J. Neiman, G. A. Wick, E. Sukovich, and B. Wang,
554 2011: Assimilation of GPS radio occultation data for an intense atmospheric river
555 with the NCEP regional GSI system. *Mon. Wea. Rev.*, 139, 2170–2183,
556 doi:10.1175/2011MWR3342.1.
- 557 Mears, C., J. Wang, S.-P. Ho, L. Zhang, and X. Zhou, 2012: Global Climate Hydrological
558 cycle, Total column water vapor [in “State of the Climate in 2011”]. *Bull. Amer.*
559 *Meteor. Soc.*, 93(7), S25–S26, doi:10.1175.
- 560 Mears, C., J. Wang, D. Smith, and F. J. Wentz, 2015: Intercomparison of total precipitable
561 water measurements made by satellite- borne microwave radiometers and ground-
562 based GPS instruments. *J. Geophys. Res. Atmos.*, 120, 2492–2504,
563 doi:10.1002/2014JD022694.
- 564 Milz, M., S. A. Buehler, and V. O. John, 2009: Comparison of AIRS and AMSU-B
565 monthly mean estimates of upper tropospheric humidity, *Geophys. Res. Lett.*, L10804,
566 doi:10.1029/2008GL037068.
- 567 Neiman, P. J., F. M. Ralph, G. A. Wick, Y.-H. Kuo, T.-K. Wee, Z. Ma, G. H. Taylor, and
568 M. D. Dettinger, 2008: Diagnosis of an intense atmospheric river impacting the Pacific
569 Northwest: Storm summary and offshore vertical structure observed with COSMIC
570 satellite retrievals. *Mon. Wea. Rev.*, 136, 4398–4420.
- 571 Noël, S., M. Buchwitz, and J. P. Burrows, 2004: First retrieval of global water vapour
572 column amounts from SCIAMACHY measurements, *Atmos. Chem. Phys.*, 4, 111–
573 125.
- 574 Palm, M., C. Melsheimer, S. Noel, J. Notholt, J. Burrows, and O. Schrems, 2008: Integrated



- 575 water vapor above Ny Alesund, Spitsbergen: a multisensor intercomparison. *Atmos.*
576 *Chem. Phys. Discuss.* 8, 21171–21199.
- 577 Pougatchev, N., T. August, X. Calbet, T. Hultberg, O. Oduleye, P. Schlüssel, B. Stiller, K.
578 St. Germain, and G. Bingham, 2009: IASI temperature and water vapor retrievals –
579 error assessment and validation. *Atmos. Chem. Phys.*, 9, 6453–6458.
- 580 Prasad, A. K. and R. P. Singh, 2009: Validation of MODIS Terra, AIRS, NCEP/DOE
581 AMIP-II Reanalysis-2, and AERONET Sun photometer derived integrated precipitable
582 water vapor using ground-based GPS receivers over India. *J. Geophys. Res.*, 114,
583 D05107, doi:10.1029/2008JD011230.
- 584 Roman, J., R. Knuteson, and S. Ackerman, 2014: Time-to-detect trends in precipitable
585 water vapor with varying measurement errors. *J. Climate*, 27, 8259–8275.
- 586 Scherllin-Pirscher, B., C. Deser, S.-P. Ho, C. Chou, W. Randel, and Y.-W. Kuo, 2012:
587 The vertical and spatial structure of ENSO in the upper troposphere and lower
588 stratosphere from GPS radio occultation measurements, *Geophys. Res. Lett.*, 39,
589 L20801, 6 PP., 2012, doi:10.1029/2012GL053071.
- 590 Schlüessel, P., & Emery, W. J. 1990: Atmospheric water vapour over oceans from SSM/I
591 measurements. *International Journal of Remote Sensing*, 11(5), 753–766.
- 592 Soden, B. J., and J. R. Lanzante, 1996: An assessment of satellite and radiosonde
593 climatologies of upper-tropospheric water vapor. *Journal of Climate*, 9(6), 1235–
594 1250.
- 595 Soden, B. J., R. T. Wetherald, G. L. Stenchikov, and A. Robock, 2002: Global cooling after
596 the eruption of Mount Pinatubo: A test of climate feedback by water
597 vapor. *Science*, 296(5568), 727–730.



- 598 Sohn, B. J., and E. A. Smith, 2003: Explaining sources of discrepancy in SSM/I water
599 vapor algorithms. *J. Climate*, 16, 3229–3255, doi:10.1175/1520-
600 0442(2003)016,3229:ESODI.2.0.CO;2.
- 601 Sohn, B.-J., and R. Bennartz, 2008: Contribution of water vapor to observational estimates
602 of longwave cloud radiative forcing, *J. Geophys. Res.*, 113, D20107,
603 doi:10.1029/2008JD010053.
- 604 Teng, W.-H., C.-Y. Huang, S.-P. Ho, Y.-H. Kuo, and X.-J. Zhou, 2013: Characteristics of
605 Global Precipitable Water in ENSO Events Revealed by COSMIC Measurements,
606 *J. Geophys. Research*, Vol. 118, 1–15, doi:10.1002/jgrd.50371.
- 607 Thompson, A., 2007: Simulating the adiabatic ascent of atmospheric air parcels using the
608 cloud chamber, Department of Meteorology, Penn State.
- 609 Trenberth K. E. and Guillemot, C. J., 1998: Evaluation of the atmospheric moisture and
610 hydrological cycle in the NCEP/NCAR reanalyses. *Clim. Dyn.*, 14:213–231
- 611 Trenberth, K.E., J. Fasullo, and L. Smith, 2005: Trends and variability in column
612 integrated atmospheric water vapor. *Climate Dynamics*, 24, 741–758.
- 613 Wang, J., L. Zhang, A. Dai, T. Van Hove, and J. Van Baelen, 2007: A near-global, 8-year,
614 2-hourly data set of atmospheric precipitable water from ground-based GPS
615 measurements. *J. Geophys. Res.*, 112, D11107, doi:10.1029/2006JD007529.
- 616 Wang, J and Zhang L. 2008: Systematic Errors in Global Radiosonde Precipitable Water
617 Data from Comparisons with Ground-Based GPS Measurements, *J. of Climate*, 21,
618 DOI:10.1175/2007JCLI1944.1.



- 619 Wang, L., X. Wu, M. Goldberg, C. Cao, Y. Li, and S.-H. Sohn, 2010: Comparison of AIRS
620 and IASI Radiances Using GOES Imagers as Transfer Radiometers toward Climate
621 Data Records. *J. Appl. Meteor. Climatol.* 49, 478–492.
- 622 Wick, G.A., Kuo, Y.-H., Ralph, F.M., Wee, T.-K., Neiman, P.J., Ma, Z, 2008:
623 Intercomparison of integrated water vapor retrievals from SSM/I and
624 COSMIC. *Geophys. Res. Lett.* 2008, 28, 3263–3266.
- 625 Wentz, F. J., 1997: A well-calibrated ocean algorithm for SSM/I. *J. Geophys.*
626 *Res.*, 102, 8703–8718.
- 627 Wentz, F. J., and R. W. Spencer, 1998: SSM/I rain retrievals within a unified all-weather
628 ocean algorithm. *J. Atmos. Sci.*, 56, 1613–1627.
- 629 Wentz, F. J., 2013: SSM/I version-7 calibration report. *Remote Sensing Systems Tech.*
630 Rep. 011012, 46 pp.
- 631 Wentz, F. J. 2015: A 17-Year climate record of environmental parameters derived from
632 the Tropical Rainfall Measuring Mission (TRMM) microwave imager, *J. Clim.*,
633 doi:10.1175/JCLI-D-15-0155.1.
- 634 Yang, S., and X. Zou, 2012: Assessments of cloud liquid water contributions to GPS RO
635 refractivity using measurements from COSMIC and CloudSat. *J. Geophys. Res.*,
636 117, D06219, doi:10.1029/2011JD016452.
- 637 Zeng, Z., S.-P. Ho, S. Sokolovskiy, 2012: The Structure and Evolution of Madden-Julian
638 Oscillation from FORMOSAT-3/COSMIC Radio Occultation Data, *J. Geophys.*
639 *Research*, 117, D22108, doi:10.1029/2012JD017685.
- 640 Zou, X., S. Yang, and P. S. Ray, 2012: Impacts of ice clouds on GPS radio occultation
641 measurements. *J. Atmos. Sci.*, 69, 3670–3682.



642

643

644

645

646

647

648

649 Table 1. Satellite Instruments Used in This Study

650

| Satellite | Instrument | Operation period |
|-----------|------------|-----------------------|
| DMSP F15 | SSM/I | December 1999-present |
| DMSP F16 | SSMIS | October 2003-present |
| DMSP F17 | SSMIS | December 2006-present |
| Coriolis | WindSat | February 2003-present |

651

652

653

654

655

656

657

658

659

660

661

662



663

664

665 Table 2: Mean and standard deviation of differences (MW minus RO) in TPW (in mm)
666 between four MW radiometers and COSMIC RO under various sky conditions. The
667 sample numbers for each pair are shown in the third position of each column.
668

669

670

671

672

673

674

675

676

677

678

679

680

681

682

683

684

685

686

687

688

689

690

691

692

693

694

695

696

697

698

699

700

701

702

703

704

705

706

| Sky condition | Mean/ σ /N | | | |
|---------------|-------------------|-----------------|-----------------|-----------------|
| | F15 | F16 | F17 | WindSat |
| Clear | 0.06/1.65/3064 | 0.03/1.47/3551 | 0.07/1.47/2888 | 0.18/1.35/1802 |
| Cloudy | 0.80/1.92/23614 | 0.79/1.73/29059 | 0.82/1.76/28403 | 0.96/1.73/20194 |
| Non Precip | 0.49/1.69/17223 | 0.46/1.46/21854 | 0.47/1.49/21371 | 0.49/1.36/13004 |
| Precip | 1.64/2.28/6391 | 1.83/2.05/7205 | 1.88/2.08/7032 | 1.85/2.00/7190 |



707

708

709

710

711 Table 3: Mean and standard deviation (std) of the mean in mm of the monthly time series
 712 of differences of MW minus RO TPW under various sky conditions. The trend of the RO
 713 estimates of TPW in mm/decade and the 95% confidence level are shown below the
 714 mean and σ values in each row.

715

716

717

| Sky condition | Mean/ σ of monthly time series RO trend (95% confidence levels indicated in ()) | | | |
|-------------------|--|--------------------------------|--------------------------------|---------------------------------|
| | F15 | F16 | F17 | WindSat |
| Clear | 0.07/0.56 1.65 (0.47,2.84) | 0.05/0.28 1.09 (-0.28,2.46) | 0.08/0.27 0.21 (-1.22,1.65) | 0.23/0.38 -0.12 (-1.89,1.66) |
| Cloudy | 0.77/0.51 1.49 (0.40,2.58) | 0.78/0.18 2.02(0.87,3.16) | 0.82/0.15 1.85 (0.64,3.06) | 0.95/0.17 1.85 (0.68,3.01) |
| Non Precipitation | 0.46/0.48 0.86 (-0.24,1.95) | 0.45/0.17 2.02 (0.87,3.17) | 0.48/0.15 2.37 (1.23,3.50) | 0.47/0.19 2.12 (0.95,3.30) |
| Precipitation | 1.62/0.69 2.52 (0.55,4.480) | 1.81/0.31 1.32 (-0.53,3.17) | 1.88/0.29 0.26 (-1.59,2.10) | 1.88/0.32 0.39 (-1.25,2.04) |

718

719

720

721

722

723

724

725

726

727

728

729

730

731

732



733

734 Figure Captions

735

736 Figure 1. The RSS V7.0 monthly mean F16 SSM/I a) TPW (in mm), b) surface skin

737 temperature (in K), c) liquid water path (LWP, in mm), and d) rain rate (RR, in

738 mm/hour).

739

740 Figure 2. TPW scatter plots for the COSMIC and RSS Version 7.0 pairs under clear

741 condition for a) F15, b) F16, c) F17, and d) WindSat.

742

743 Figure 3. TPW scatter plots for the COSMIC and RSS Version 7.0 F16 SSM/I pairs

744 under a) cloudy, b) cloudy but non-precipitation, and c) precipitation conditions.

745

746 Figure 4. TPW scatter plots for the gb-GPS and RSS Version 7.0 F16 SSM/I pairs from

747 June 2006 to December 2013 under a) clear, b) cloudy, c) cloudy but non-precipitation,

748 and d) precipitation conditions.

749

750 Figure 5. Mean and standard of the mean for the F16-COSMIC TPW biases varying with

751 a) wind speed (m/s), b) TPW (mm), c) rain rate (mm/hour), d) total cloud water (mm),

752 and e) surface skin temperature (K). The vertical black bracket superimposed on the

753 mean denotes the standard error of the mean. The green dashed line is the number of

754 samples, indicated by the scale on the right.

755



756 Figure 6. Mean and standard of the mean for the F16- gb-GPS TPW biases varying with
757 a) wind speed (m/s), b) TPW (mm), c) rain rate (mm/hour), d) total cloud water (mm) and
758 e) surface skin temperature (K). The vertical black bracket superimposed on the mean
759 denotes the standard error of the mean. The green dashed line is the number of samples,
760 indicated by the scale on the right.

761

762 Figure 7. The time series of monthly mean F16 – COSMIC TPW differences under a)
763 clear, b) cloudy, c) cloudy but non-precipitation, and d) precipitation conditions. The
764 black line is the mean difference for microwave radiometer minus COSMIC; the vertical
765 lines superimposed on the mean values are the standard error of the mean. The number of
766 the monthly MW radiometer- COSMIC pairs is indicated by the green dashed line (scale
767 on the right Y axis).

768

769 Figure 8. The time series of de-seasonalized TPW differences (microwave radiometer –
770 COSMIC) under cloudy skies for a) F15, b) F16, c) F17, d) WindSat. The black line is
771 the mean difference for microwave radiometer minus COSMIC; the vertical lines
772 superimposed on the mean values are the standard error of the mean. The number of the
773 monthly MW radiometer- COSMIC pairs is indicated by the green dashed line (scale on
774 the right Y axis). The trends are shown by solid red line. The 95% confidence intervals
775 for slopes are shown in the parentheses.

776



777 Figure 9. The de-seasonalized time series of global monthly mean TPW for all MW
778 instruments and COSMIC under all sky conditions. The red and blue dashed lines are the
779 best fit of de-seasonalized COSMIC and MW TPW time series, respectively.

780

781 Figure 10. The global map of TPW trend over oceans using all F16, F17, Windsat data
782 from 2006 to 2013.

783

784

785

786

787

788

789

790

791

792

793

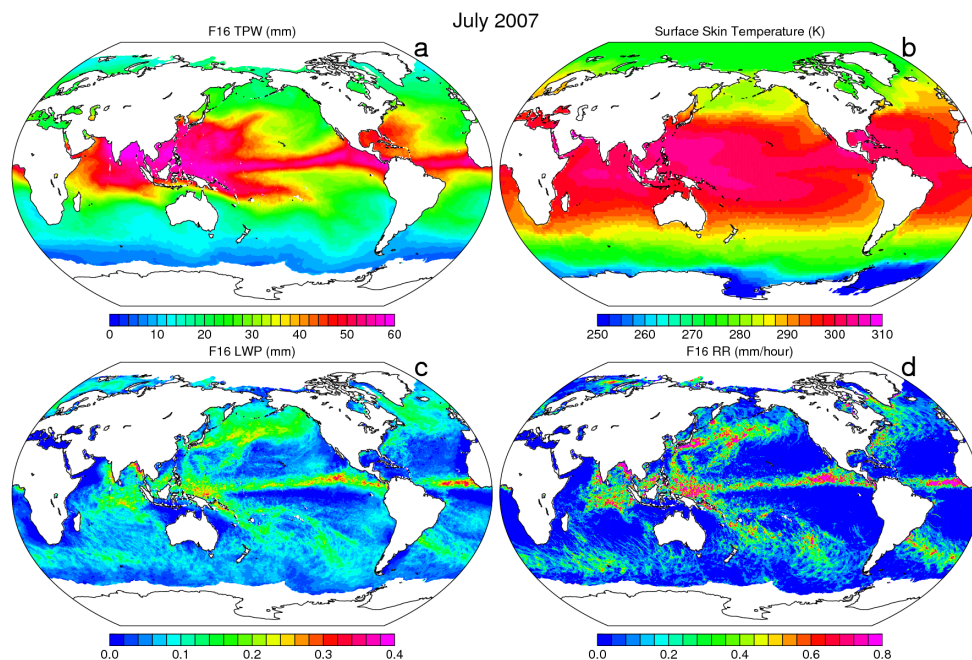
794

795

796

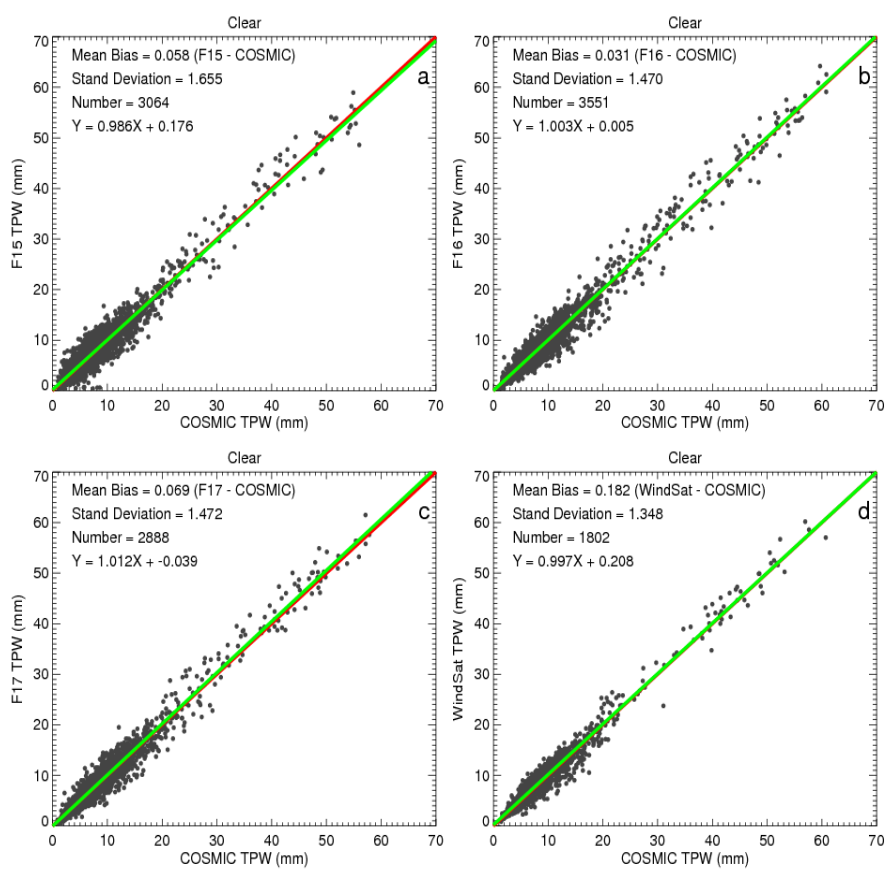
797

798



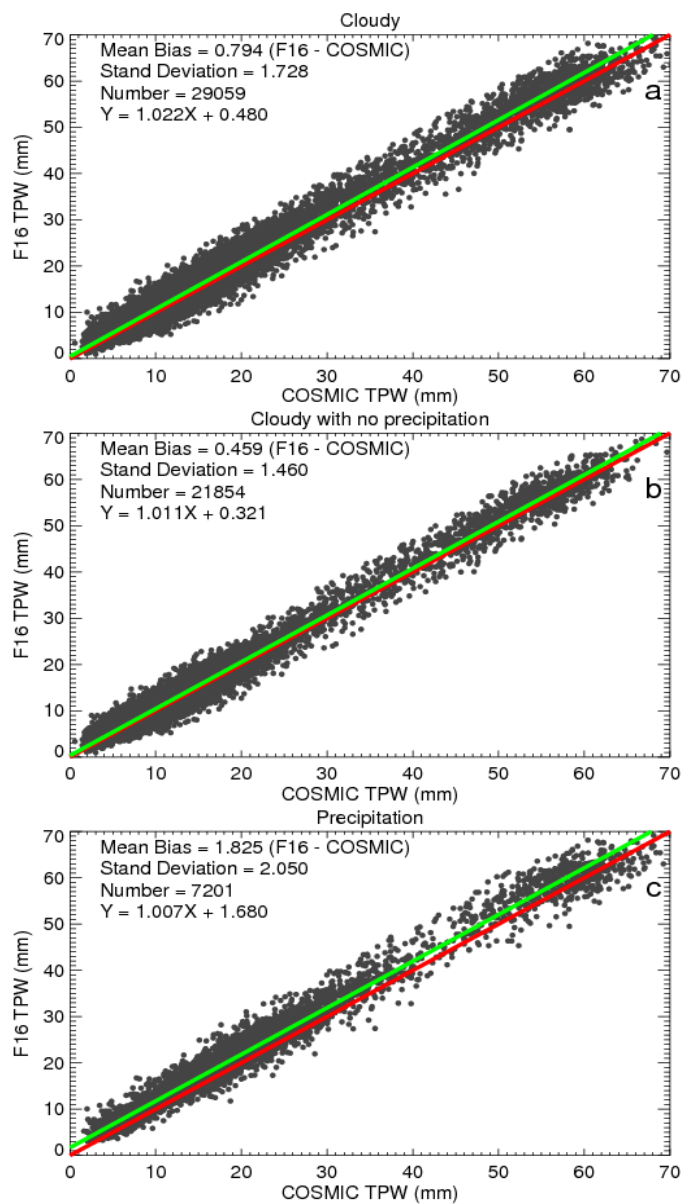
799
800
801
802
803
804
805
806
807
808
809
810
811
812
813
814
815
816
817
818
819
820
821
822
823

Figure 1. The RSS V7.0 monthly mean F16 SSM/I a) TPW (in mm), b) surface skin temperature (in K), c) liquid water path (LWP, in mm), and d) rain rate (RR, in mm/hour).



824
825
826
827
828
829
830
831
832
833
834

Figure 2. TPW scatter plots for the COSMIC and RSS Version 7.0 pairs under clear condition for a) F15, b) F16, c) F17, and d) WindSat.



835

836

837 Figure 3. TPW scatter plots for the COSMIC and RSS Version 7.0 F16 SSM/I pairs

838 under a) cloudy, b) cloudy but non-precipitation, and c) precipitation conditions.

839

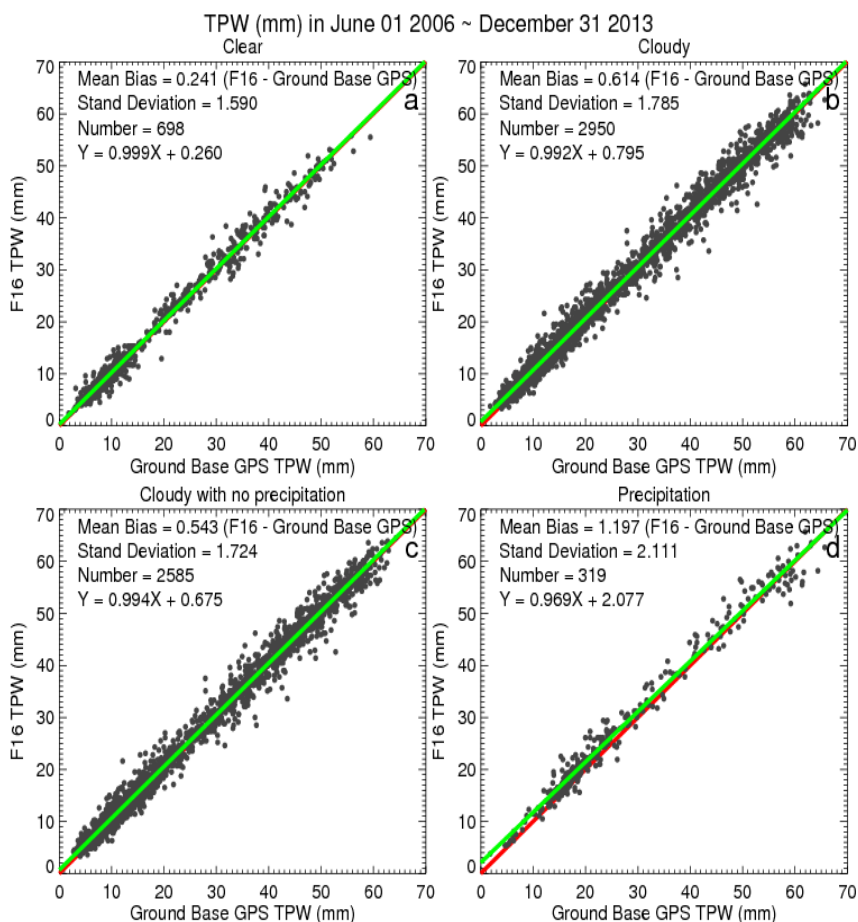
840

841

842



843
844

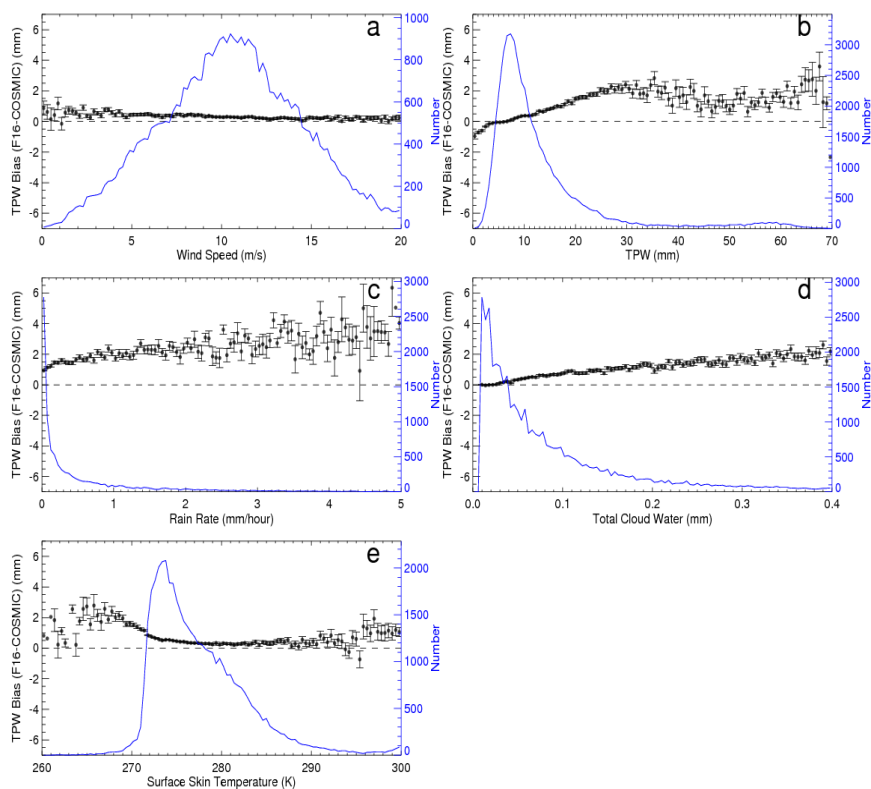


845
846
847
848
849
850
851
852
853
854
855
856
857
858
859
860

Figure 4. TPW scatter plots for the gb-GPS and RSS Version 7.0 F16 SSM/I pairs from June 2006 to December 2013 under a) clear, b) cloudy, c) cloudy but non-precipitation, and d) precipitation conditions.



861
862

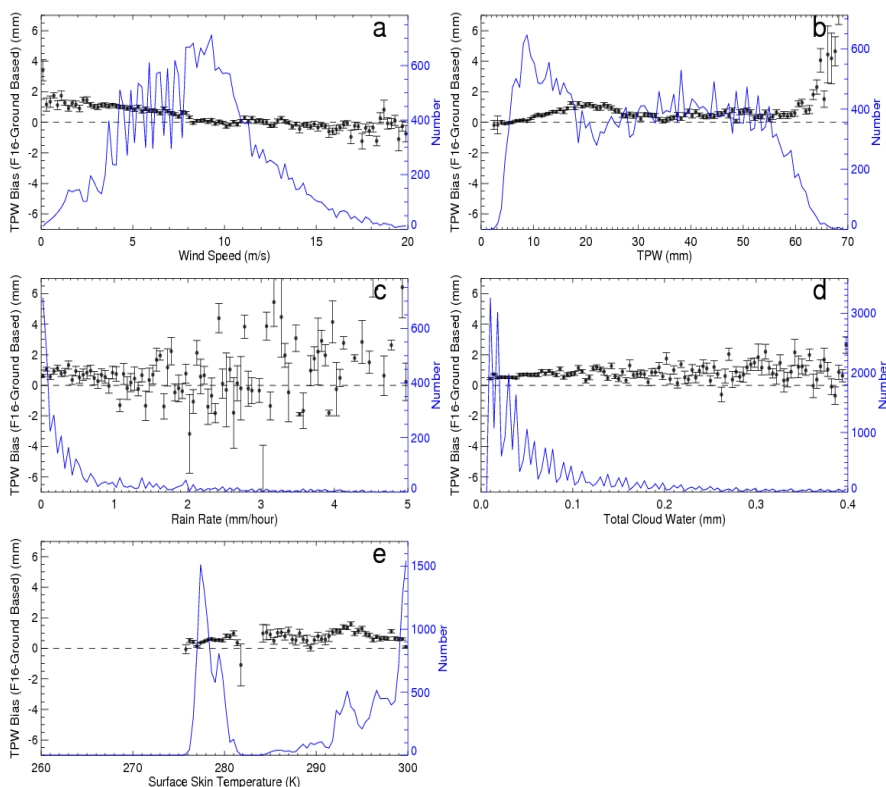


863
864
865
866
867
868
869
870
871
872
873
874
875
876
877
878
879
880
881
882

Figure 5. Mean and standard of the mean for the F16-COSMIC TPW biases varying with a) wind speed (m/s), b) TPW (mm), c) rain rate (mm/hour), d) total cloud water (mm), and e) surface skin temperature (K). The vertical black bracket superimposed on the mean denotes the standard error of the mean. The green dashed line is the number of samples, indicated by the scale on the right.



883
884
885
886
887

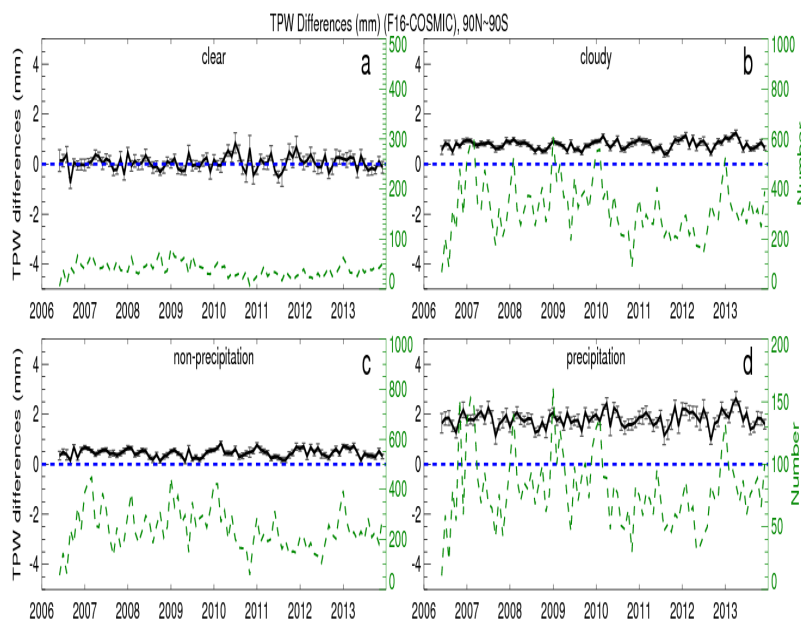


888
889
890
891
892
893
894
895
896
897
898
899
900
901
902
903
904

Figure 6. Mean and standard of the mean for the F16- gb-GPS TPW biases varying with a) wind speed (m/s), b) TPW (mm), c) rain rate (mm/hour), d) total cloud water (mm) and e) surface skin temperature (K). The vertical black bracket superimposed on the mean denotes the standard error of the mean. The green dashed line is the number of samples, indicated by the scale on the right.

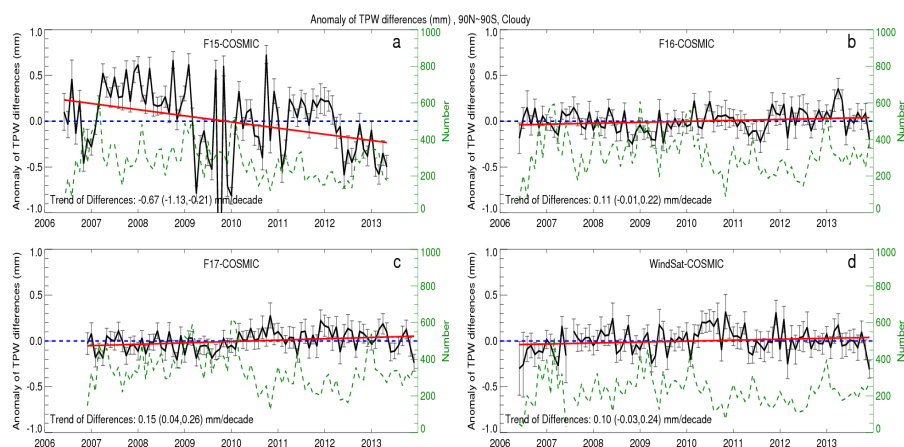


905
906
907



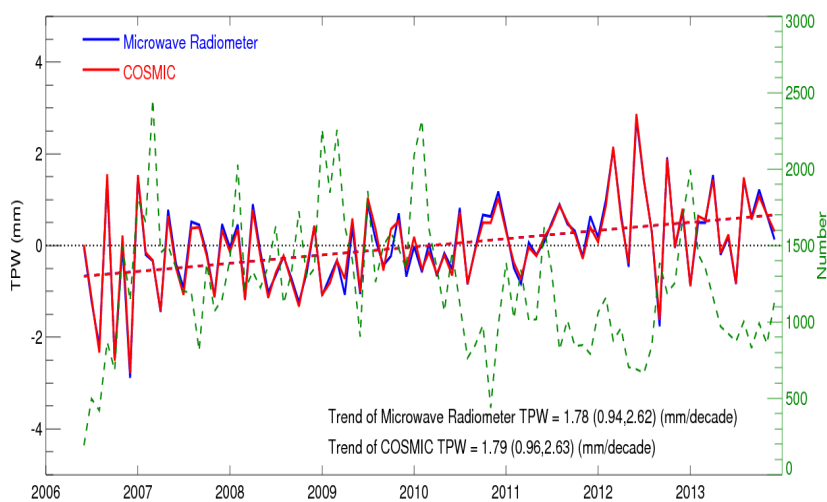
908
909
910
911
912
913
914
915
916
917
918
919
920
921
922

Figure 7. The time series of monthly mean F16 – COSMIC TPW differences under a) clear, b) cloudy, c) cloudy but non-precipitation, and d) precipitation conditions. The black line is the mean difference for microwave radiometer minus COSMIC; the vertical lines superimposed on the mean values are the standard error of the mean. The number of the monthly MW radiometer- COSMIC pairs is indicated by the green dashed line (scale on the right Y axis).



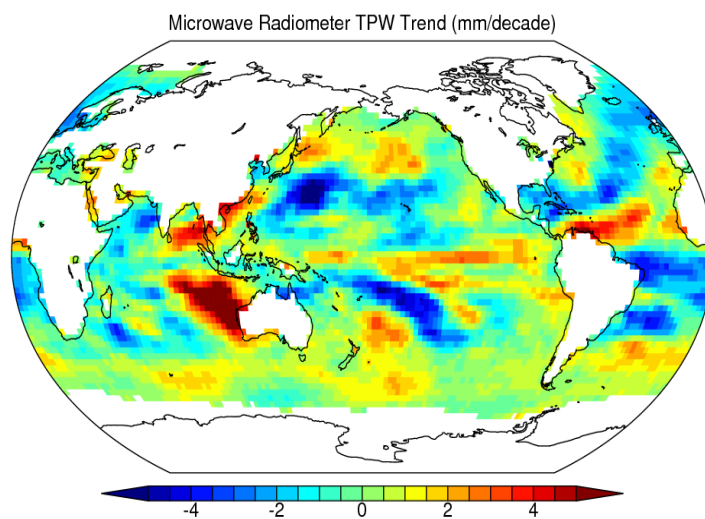
923
924
925
926
927
928
929
930
931
932
933
934
935
936
937
938
939
940
941
942
943
944
945
946
947

Figure 8. The time series of de-seasonalized TPW differences (microwave radiometer – COSMIC) under cloudy skies for a) F15, b) F16, c) F17, d) WindSat. The black line is the mean difference for microwave radiometer minus COSMIC; the vertical lines superimposed on the mean values are the standard error of the mean. The number of the monthly MW radiometer- COSMIC pairs is indicated by the green dashed line (scale on the right Y axis). The trends are shown by solid red line. The 95% confidence intervals for slopes are shown in the parentheses.



948
949
950
951
952
953
954
955
956
957
958
959
960
961
962
963
964
965
966
967
968
969
970
971

Figure 9. The de-seasonalized time series of global monthly mean TPW for all MW instruments and COSMIC under all sky conditions. The red and blue dashed lines are the best fit of de-seasonalized COSMIC and MW TPW time series, respectively.



972
973
974
975
976
977

Figure 10. The global map of TPW trend over oceans using all F16, F17, Windsat data from 2006 to 2013.